

1 **Easy-to-use spatial Random Forest-based downscaling-calibration method for**
2 **producing precipitation data with high resolution and high accuracy**

3 Chuanfa Chen^{1,2}, Baojian Hu^{1,2}, Yanyan Li^{1,2}

4 ¹ College of Geodesy and Geomatics, Shandong University of Science and Technology, Qingdao
5 266590, China

6 ² Key Laboratory of Geomatics and Digital Technology of Shandong Province, Shandong University of
7 Science and Technology, Qingdao 266590, China

8 *Correspondence to:* Yanyan Li (yylee@whu.edu.cn)

9 **Abstract.** Precipitation data with high resolution and high accuracy is significantly important in
10 numerous hydrological applications. To enhance the spatial resolution and accuracy of satellite-based
11 precipitation products, an easy-to-use downscaling-calibration method based on spatial Random Forest
12 (SRF-DC) is proposed in this study, where the spatial correlation of precipitation measurements
13 between neighboring locations is considered. SRF-DC consists of two main stages. First, the
14 satellite-based precipitation is downscaled by SRF with the incorporation of high-resolution variables
15 including latitude, longitude, Normalized Difference Vegetation Index (NDVI), digital elevation model
16 (DEM), terrain slope, aspect, relief, and land surface temperatures. Then, the downscaled precipitation
17 is calibrated by SRF with rain gauge observations and the aforementioned high-resolution variables.
18 The monthly Integrated MultisatellitE Retrievals for Global Precipitation Measurement (IMERG) over
19 Sichuan province, China from 2015 to 2019 was processed using SRF-DC, and its results were
20 compared with those of classical methods including geographically weighted regression (GWR),
21 artificial neural network (ANN), random forest (RF), kriging interpolation only on gauge
22 measurements, bilinear interpolation-based downscaling and then SRF-based calibration (Bi-SRF), and
23 SRF-based downscaling and then geographical difference analysis (GDA)-based calibration
24 (SRF-GDA). Comparative analyses with respect to root mean square error (RMSE), mean absolute
25 error (MAE) and correlation coefficient (CC) demonstrate that: (1) SRF-DC outperforms the classical
26 methods as well as the original IMERG; (2) the monthly-based SRF estimation is slightly more
27 accurate than the annual-based SRF fraction disaggregation method; (3) SRF-based downscaling and
28 calibration performs better than bilinear downscaling (Bi-SRF) and GDA-based calibration
29 (SRF-GDA); (4) kriging is more accurate than GWR and ANN, whereas its precipitation map loses

30 detailed spatial precipitation patterns; and (5) based on the variable importance rank of RF, the
31 precipitation interpolated by kriging on the rain gauge measurements is the most important variable,
32 indicating the significance of incorporating spatial autocorrelation for precipitation estimation.

33 **1. Introduction**

34 Precipitation is an important variable for promoting our understanding of hydrological cycle and
35 water resource management (Chen et al., 2010). Previous studies have showed that about 70-80% of
36 hydrological modeling errors are caused by precipitation uncertainties (Gebregiorgis and Hossain,
37 2013). However, precipitation is also one of the most difficult meteorological factors to estimate due to
38 its high spatial and temporal heterogeneity (Beck et al., 2019). Although point-based rain gauge
39 observations are reliable and accurate, it is difficult to reflect the spatial precipitation pattern because of
40 the sparse and uneven distribution of meteorological stations, especially in remote and mountainous
41 areas (Ullah et al., 2020).

42 During the past decades, diverse satellite-based precipitation datasets have been produced, such as
43 the Climate Hazards Group Infrared Precipitation with Station data (CHIRPS, 0.05°) (Funk et al.,
44 2015), the Precipitation Estimation from Remotely Sensed Information using Artificial Neural
45 Networks-Climate Data Record (PERSIANN-CDR, 0.25°) (Ashouri et al., 2015), the Climate
46 Prediction Center (CPC) morphing technique (CMORPH, 0.25°) (Haile et al., 2013), the Multi-Source
47 Weighted-Ensemble Precipitation (MSWEP, 0.1°) (Beck et al., 2017), the Tropical Rainfall Measuring
48 Mission (TRMM) Multi-satellite Precipitation Analysis (TMPA, 0.25°) (Huffman et al., 2007) and the
49 Integrated MultisatellitE Retrievals for Global Precipitation Measurement (GPM) mission (IMERG,
50 0.1°) (Hou et al., 2014). Nevertheless, these products are characterized by considerable systematic
51 biases due to the shortcomings of retrieval algorithms, sensor capability and spatiotemporal collection
52 frequency (Chen et al., 2018; Wu et al., 2018; Yang et al., 2017). Moreover, their resolutions (from 0.05°
53 to 2.5°) are too coarse for hydrological modeling when applied to local and basin regions (Immerzeel et
54 al., 2009).

55 As a result, downscaling techniques have been widely adopted to derive high resolution precipitation
56 products. This is generally achieved by firstly modeling the relationship between precipitation and land
57 surface variables at a coarse scale, and then putting the high resolution variables into the constructed

58 model to downscale the precipitation data (Immerzeel et al., 2009; Chen et al., 2010). Immerzeel et al.
59 (2009) employed an exponential regression (ER) to describe the relationship between TRMM and
60 Normalized Difference Vegetation Index (NDVI). Jia et al. (2011) used a multiple linear regression
61 model (MLR) to establish the relationship between TRMM, digital elevation model (DEM) and NDVI.
62 Duan and Bastiaanssen (2013) proposed a downscaling model based on the second-order polynomial
63 relationship between TRMM and NDVI. Considering the heterogeneous relationships between
64 precipitation and land surface variables across the study area, geographically weighted regression
65 (GWR) was widely used (Chen et al., 2014; Chen et al., 2015; Xu et al., 2015; Li et al., 2019; Chen et
66 al., 2020c; Lu et al., 2020; Zhao et al., 2018). In the recent decade, some data-driven machine learning
67 (ML) methods were employed to downscale satellite-based precipitation products, such as random
68 forest (RF) (Shi et al., 2015; Zhang et al., 2021), support vector machine (SVM) (Jing et al., 2016;
69 Chen et al., 2010) and artificial neural network (ANN) (Elnashar et al., 2020), and showed more
70 accurate results than the statistical methods. However, the downscaled precipitation products inherently
71 contain large systematic biases.

72 To alleviate the inherent biases, many calibration methods have been proposed to merge gauge
73 observations and satellite-based precipitation, such as nonparametric kernel smoothing method (Li and
74 Shao, 2010), geographical difference analysis (GDA) (Cheema and Bastiaanssen, 2012), geographical
75 ratio analysis (GRA) (Duan and Bastiaanssen, 2013), conditional merging (CM) (Berndt et al., 2014),
76 quantile mapping (Chen et al., 2013; Zhang and Tang, 2015), optimal interpolation (Xie and Xiong,
77 2011; Lu et al., 2020; Wu et al., 2018), GWR (Chen et al., 2018; Lu et al., 2019; Chao et al., 2018) and
78 geostatistical interpolation (Park et al., 2017). Nevertheless, these methods are based on some strict
79 assumptions, which might be not satisfied in reality (Zhang et al., 2021; Wu et al., 2020). To this end,
80 ML-based calibration methods have been widely used, such as Quantile Regression Forest (QRF)
81 (Bhuiyan et al., 2018), ANN (Yang and Luo, 2014; Pham et al., 2020), deep neural network (Tao et al.,
82 2016), RF (Baez-Villanueva et al., 2020), convolutional neural network (CNN) (Wu et al., 2020), SVM
83 and extreme learning machine (Zhang et al., 2021).

84 Compared to the statistical methods, the merits of the ML-based methods are as follows (Zhang et al.,
85 2021; Hengl et al., 2018): (i) they require no strict statistical assumption; (ii) they can capture the
86 complex and nonlinear relationship between precipitation and its influence factors; (iii) they generally

87 outperform the statistical methods. However, ML-based methods were simply taken as statistical tools
88 without considering the spatial autocorrelation of precipitation measurements between adjacent
89 locations. Moreover, they were adopted in either downscaling or calibration of precipitation.
90 Specifically, some (Karbalaye Ghorbanpour et al., 2021; Yan et al., 2021; Jing et al., 2016) attempted to
91 use the ML methods for downscaling and then use the classical method (e.g. GDA) for calibration,
92 while some (Zhang et al., 2021) employed the classical interpolation methods (e.g. bilinear
93 interpolation) for downscaling and then used the ML methods for calibration. However, we regard that
94 the use of ML methods in both downscaling and calibration could improve the accuracy of
95 precipitation. To the best of our knowledge, no previous studies have used the ML technique in both
96 downscaling and calibration (Karbalaye Ghorbanpour et al., 2021; Yan et al., 2021).

97 Based on aforementioned discussion, the objectives of this study are twofold: (i) to develop an
98 easy-to-use spatial RF (SRF) by incorporating spatial autocorrelation for precipitation estimation, and
99 (ii) to propose a downscaling-calibration method based on SRF (SRF-DC) for producing high
100 resolution and high accuracy precipitation products. RF is taken as the basic model in this study owing
101 to its high interpolation accuracy and low computational cost (Mohsenzadeh Karimi et al., 2020;
102 Belgiu et al., 2016).

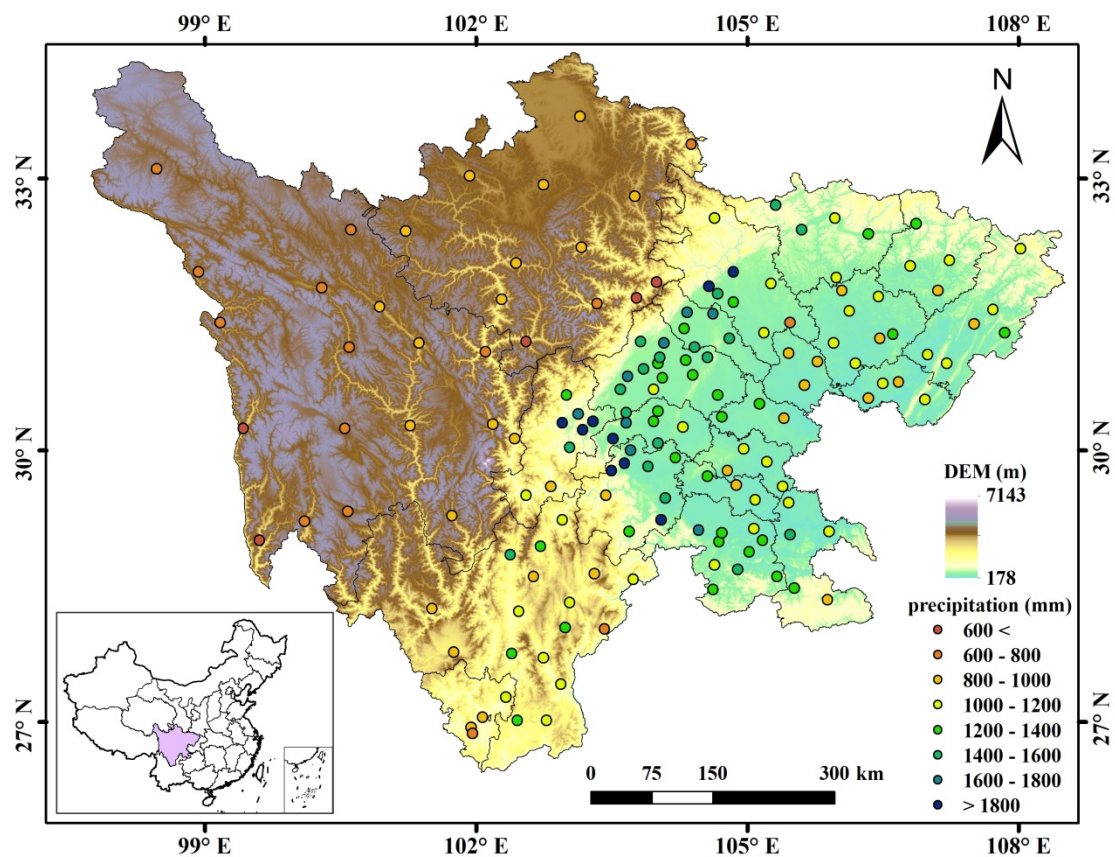
103 SRF-DC consists of two main steps. First, the precipitation data is downscaled by SRF with the
104 incorporation of high resolution environmental variables, including DEM, NDVI, land surface
105 temperatures (LSTs), terrain parameters, latitude and longitude, as recommended in previous studies
106 (Jing et al., 2016; Li et al., 2019). Second, SRF and the environmental variables are further used to
107 merge the downscaled precipitation data and gauge observations to boost the accuracy of the
108 precipitation data. The merit of SRF-DC lies in the use of SRF for both downscaling and calibration of
109 precipitation products, with the incorporation of high-resolution environmental variables.

110 **2 Study area and dataset**

111 **2.1. Study area**

112 Sichuan province between 97°21'-108°31'E and 26°03'-34°19'N (Fig. 1) is situated between the
113 Qinghai-Tibet Plateau and the Plain of the Middle-and-lower Reaches of Yangtze River, with an area of

114 486,000 km². Its topography is very complex, including mountains, hills, plain basins and plateaus, and
 115 the elevations range from approximately 180 m in the east to 7100 m in the west. Such a variety of
 116 complex topography results in different climate across the study region. Specifically, the east basin has
 117 subtropical monsoon climate. The weather is generally warm, humid and foggy with much cloud, fog
 118 and rain but less sunshine. While in the west plateau, the weather is relatively cool or cold. The climate
 119 is featured by a long cold winter, a very short summer and rich sunshine but less rainfall. Annual
 120 precipitation shows significant spatial heterogeneity, varying from about 400 mm in the west to 1800
 121 mm in the east. Moreover, more than 80% precipitation occurs between July and September. The high
 122 spatial and temporal variability of precipitation makes the study site ideal for evaluating satellite-based
 123 precipitation estimates (Zhang et al., 2021; Karbalaye Ghorbanpour et al., 2021).



124

125 Fig. 1 Topography, rain gauges and geographic location of Sichuan province in China

126

126 2.2. Dataset

127

127 2.2.1. Rain gauge observations

128

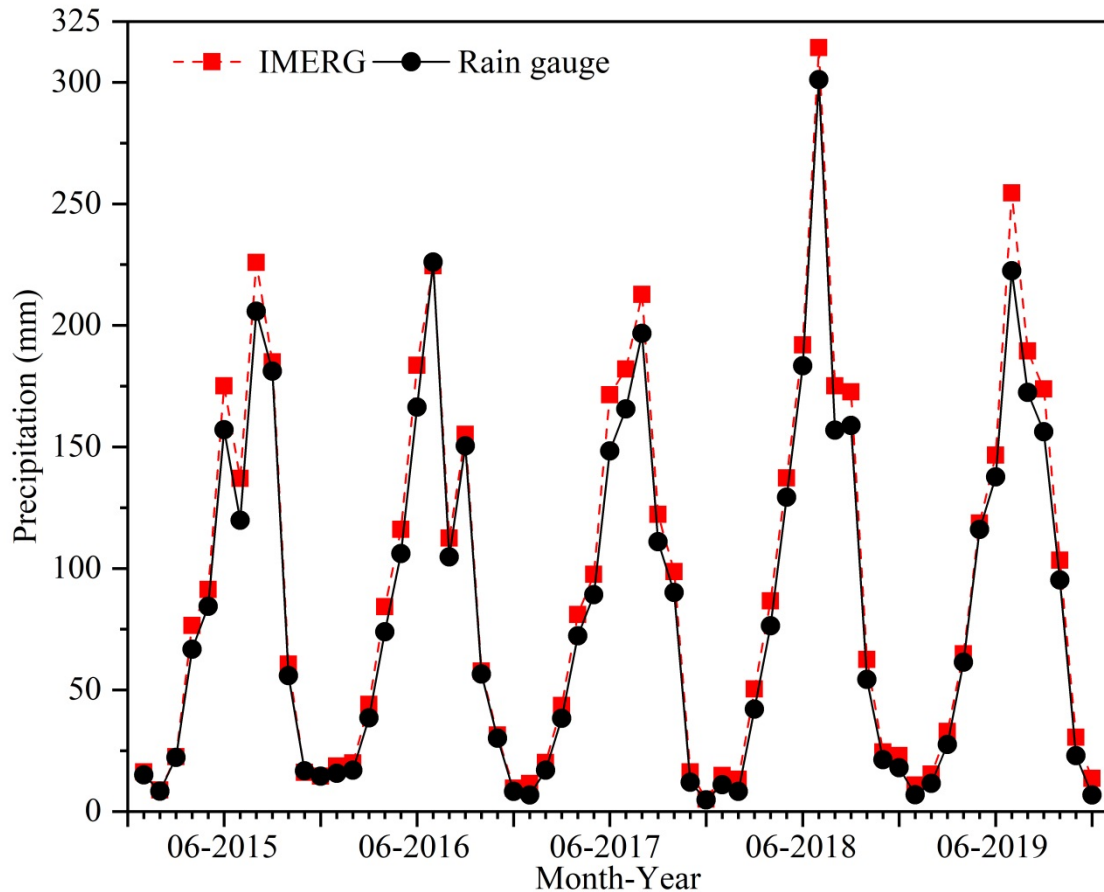
The study region has 156 rain gauge stations, which shows an uneven distribution with high density

129 in the east and low density in the west (Fig. 1). The average cover area of one rain gauge observation is
130 about 3115 km². Daily precipitation of all the stations for the period 2015–2019 was collected from the
131 China Meteorological Data Service Center (CMDSC, <http://data.cma.cn/>). The data quality was
132 guaranteed based on some strict quality controls, such as manual inspection, outlier check and
133 spatiotemporal consistency verification (Zhao and Yatagai, 2014). After that, the monthly precipitation
134 was produced by aggregating the daily precipitation of rain gauges for each month.

135 2.2.2. Integrated MultisatellitE Retrievals for Global Precipitation Measurement (IMERG)

136 As the successor of TRMM, the National Aeronautics and Space Administration (NASA) and the
137 Japan Aerospace Exploration Agency (JAXA) initiated the next-generation global precipitation
138 observation mission (Hou et al., 2014). The IMERG products were generated by assimilating all
139 microwave and infrared (IR) estimates, together with gauge observations (Huffman et al., 2019). It has
140 the spatial resolution of 0.1° × 0.1° with the coverage from 60°S–60°N. IMERG provides three
141 different products including Early, Late, and Final Runs, which were estimated about 4 hours, 14 hours,
142 and 3.5 months after observation time, respectively. Due to the incorporation of the Global
143 Precipitation Climatology Centre (GPCC) rain gauge data, IMERG Final Run is more accurate than the
144 others (Lu et al., 2019). Thus, the monthly IMERG V06B Final Run product was adopted in the study.
145 It was downloaded from <https://gpm.nasa.gov/data/>.

146 The average monthly precipitation of all rain gauges and that of IMERG at the corresponding grid
147 cells from 2015–2019 over Sichuan province are shown in Fig. 2. Obviously, IMERG has an
148 overestimation in most months and the wettest month is July 2018.



149

150 Fig. 2 Average monthly precipitation of all rain gauges and that of IMERG at the corresponding grid
 151 cells from 2015-2019 over Sichuan province

152 2.2.3. Environmental variables

153 Vegetation types have a significant impact on fluxes of sensible and latent heat into the atmosphere,
 154 apparently influencing the humidity of the lower atmosphere and further affecting moist convection
 155 (Spracklen et al., 2012). Therefore, as an indicator of vegetation activity, NDVI has been widely
 156 adopted to estimate precipitation (Wu et al., 2019; Immerzeel et al., 2009). In this study, the Moderate
 157 Resolution Imaging Spectroradiometer (MODIS) monthly NDVI with the resolution of 1 km
 158 (MOD13A3) from 2015 to 2019 (<https://search.earthdata.nasa.gov/>) was used.

159 Precipitation can influence LTS both in the daytime and at night; rain leads to cool temperatures,
 160 and droughts often couple with heat waves (Trenberth and Shea, 2005; Jing et al., 2016). Thus, the
 161 daytime LST (LST_D), nighttime LST (LST_N), and the difference between daytime and nighttime LSTs
 162 (LST_{D-N}) at the monthly scale were used in this study. Here, MODIS 8-day LST with the resolution of 1
 163 km (MOD11A2) from 2015 to 2019 was downloaded from <https://ladsweb.modaps.eosdis.nasa.gov/>
 164 and then temporally averaged into the monthly LST products.

165 Topography could affect the regional atmospheric circulation and the spatial pattern of precipitation
 166 through its thermal and dynamic forcing mechanisms (Jing et al., 2016; Jia et al., 2011). With the
 167 increase of elevations, the relative humidity of the air masses increases through expansion and cooling
 168 of the rising air masses, which could bring precipitation (Jing et al., 2016). Thus, the
 169 precipitation-DEM relationship has been widely employed to downscale satellite precipitation dataset.
 170 Here, the Shuttle Radar Topography Mission (SRTM) DEM (Shortridge and Messina, 2011) was used.
 171 The SRTM DEM with the spatial resolution of 90 m was downloaded from <http://srtm.csi.cgiar.org/>
 172 and then resampled to 1 km by the pixel averaging method. Since precipitation tends to be influenced
 173 by terrain variability, DEM derivatives including slope, aspect and terrain relief (Chen et al., 2020a)
 174 were also used in the study. These derivatives were extracted from the SRTM DEM using ArcGIS 10.3.

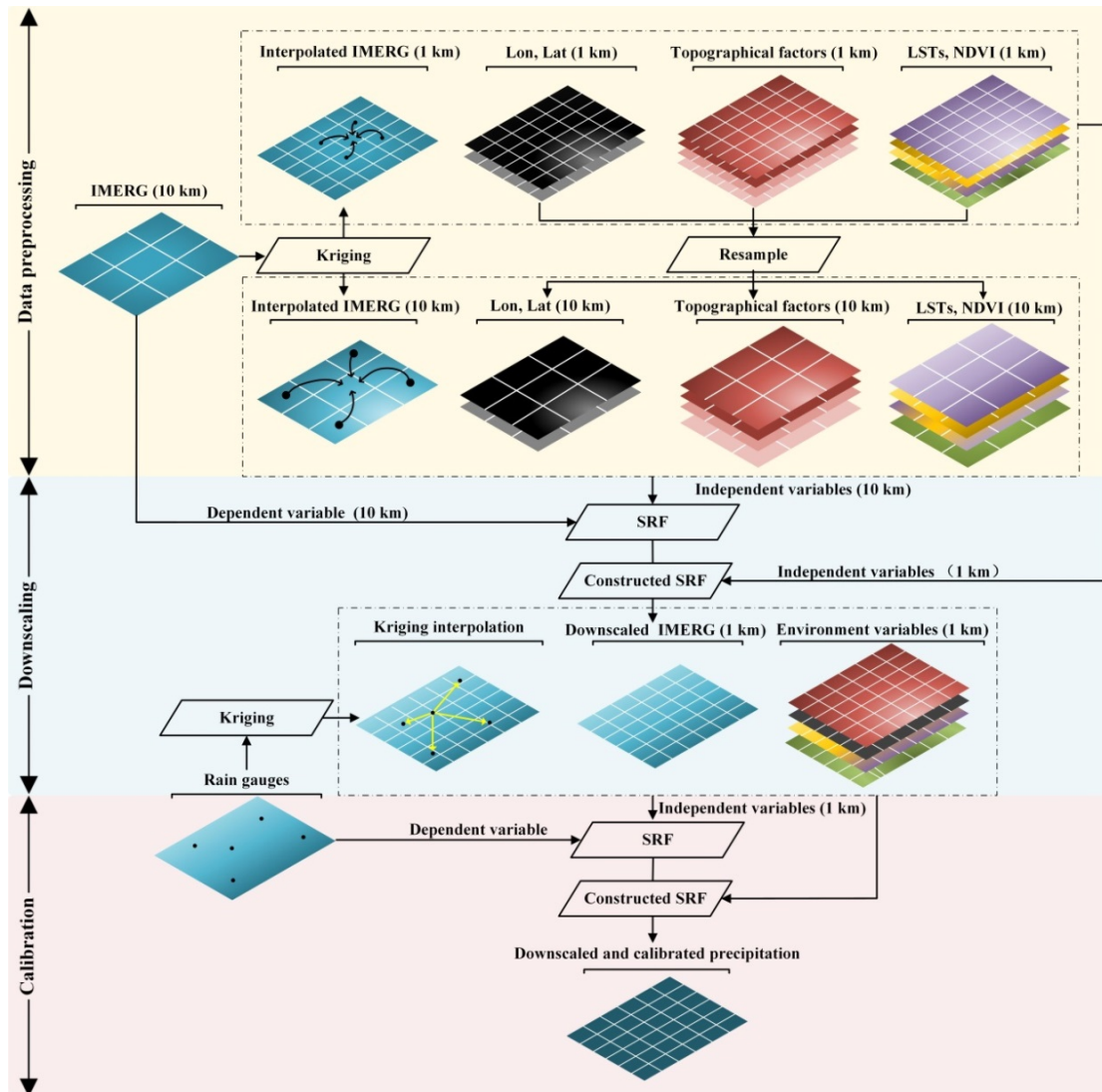
175 The detailed information of all the datasets used in the study is shown in Table 1.

176 Table 1 Datasets used in the study

Data Type	Product	Spatial resolution	Temporal resolution	Source
Meteorological data	IMERG	10 km	Monthly	https://gpm.nasa.gov/data .
	Rain gauge observations	-	Daily	http://data.cma.cn/
Land surface data	SRTM DEM	30 m	-	http://srtm.csi.cgiar.org/
	slope, aspect, terrain relief	30 m	-	Derived from SRTM DEM
	NDVI	1 km	Monthly	https://search.earthdata.nasa.gov/
	LST	1 km	8-days	https://ladsweb.modaps.eosdis.nasa.gov

177 3. Methodology

178 The flowchart of SRF-DC is illustrated in Fig. 3, which includes three stages: data processing,
 179 IMERG downscaling and downscaled IMERG calibration. It is noted that each IMERG pixel
 180 represents the areal average precipitation within it, whereas rain gauge measurements are point-based.
 181 Therefore, downscaling before calibration can decrease scale mismatch between pixel-based areal
 182 precipitation and gauge-based point measurements.



183

184

Fig. 3 Flowchart of SRF-DC in this study

185

3.1. Random Forest (RF)

186

RF is an ensemble of several tree predictors such that each tree relies on a random and independent selection of some samples and features but with the same distribution (Breiman, 2001). The general framework of RF is shown in Fig. 4. Specifically, each decision tree is constructed by randomly collecting some training data with replacement, while the others are used to assess the tree performance (sample bagging). When constructing each tree, only a random subset of features is selected at each decision node (feature bagging). In the end, the majority vote for classification or the average prediction of all trees for regression is used to obtain the final output. Overall, RF includes three parameters to set: number of trees, depth of the tree, and number of features.

193

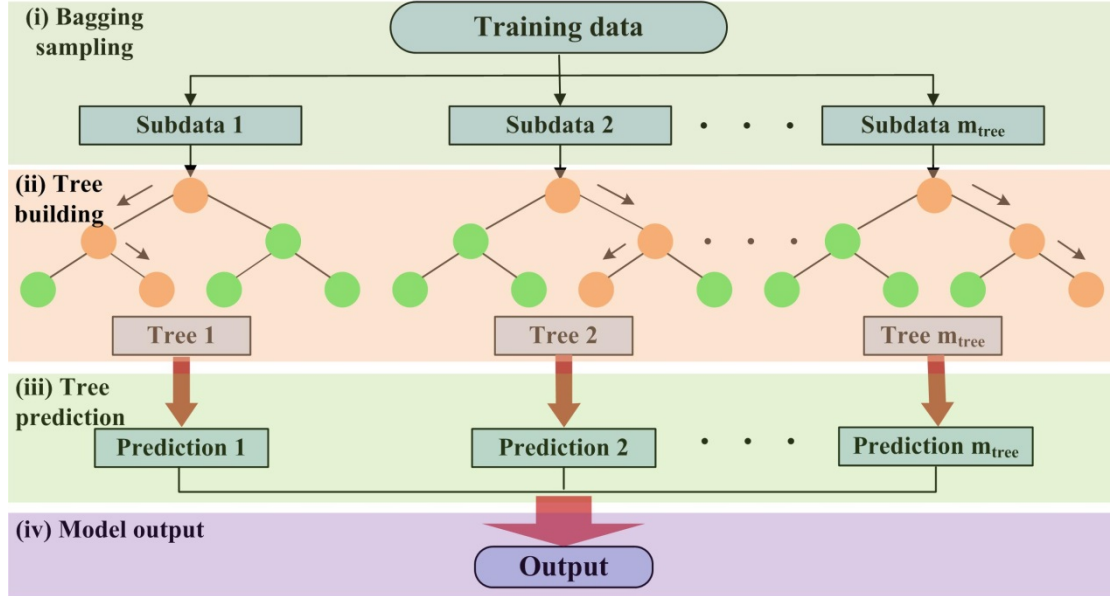


Fig. 4 General framework of RF

Meanwhile, RF can evaluate the relative importance of each predictor by means of the out-of-bag (OOB) observations, i.e. the samples without being used for model construction. Specifically, to measure the importance of the i th predictor, its values are permuted while the values of the other predictors remain unchanged. Then, the OOB error based on the permuted samples is computed. Next, the importance score of the i th predictor is computed by averaging the difference between the OOB errors before and after the permutation. With the estimated scores, the importance of each variable is ranked.

In this study, the RF regression model was performed with the freely available codes, downloaded from the website (<https://code.google.com/archive/p/randomforest-matlab/downloads>).

3.2. Spatial Random Forest (SRF)

In essence, the classical RF is a non-spatial statistical technique for spatial prediction, as it neglects sampling locations and general sampling pattern (Hengl et al., 2018). This can potentially cause sub-optimal estimations, especially when the spatial autocorrelation between dependent variables is high. To this end, a spatial RF (SRF) is proposed in this study. The general formulation of SRF is as follows:

$$p(s_0) = f(\mathbf{X}_s, \mathbf{X}_{ns}) + e \quad (1)$$

where $p(s_0)$ is the estimated precipitation at location s_0 , e is the fitting residual, $f(\bullet)$ is the function

213 constructed by SRF, and \mathbf{X}_s and \mathbf{X}_{ns} are the spatial and non-spatial covariates, respectively.

214 In addition to spatial coordinates, one spatial covariate (X_s) is computed to account for the spatial
215 autocorrelation of precipitation measurements between neighboring locations:

$$216 \quad X_s(s_0) = \sum_{i=1}^n w_i z(s_i) \quad (2)$$

217 where s_i is the i th neighbor of s_0 , $z(s_i)$ is the precipitation data of s_i , w_i is its weight, and n is the number
218 of neighbors.

219 In previous studies (Zhang et al., 2021; Li et al., 2017), the inverse distance weights (IDW) were
220 widely used. However, the IDW method only resorts to the spatial distance between the estimated
221 location and its neighbor locations, and does not consider the spatial autocorrelation between the
222 neighboring locations. To overcome this limitation, ordinary kriging (OK)-based variogram is adopted
223 to estimate the interpolation weights in this study by solving the following linear system:

$$224 \quad \begin{pmatrix} \gamma(\mathbf{x}_1 - \mathbf{x}_1) & \cdots & \gamma(\mathbf{x}_1 - \mathbf{x}_n) & 1 \\ \vdots & \ddots & \vdots & \vdots \\ \gamma(\mathbf{x}_n - \mathbf{x}_1) & \cdots & \gamma(\mathbf{x}_n - \mathbf{x}_n) & 1 \\ 1 & \cdots & 1 & 0 \end{pmatrix} \begin{pmatrix} w_1 \\ \vdots \\ w_n \\ \mu \end{pmatrix} = \begin{pmatrix} \gamma(\mathbf{x}_1 - \mathbf{x}_0) \\ \vdots \\ \gamma(\mathbf{x}_n - \mathbf{x}_0) \\ 1 \end{pmatrix} \quad (3)$$

225 where μ is Lagrange parameter and $\gamma(\cdot)$ is the semivariogram.

226 It can be concluded that the variogram-based weights consider the spatial autocorrelation not only
227 between the known locations, but also between the known locations and the interpolated location
228 (Berndt and Haberlandt, 2018). In practice, the experimental semivariogram can be estimated from
229 sample data as follows (Goovaerts, 2000):

$$230 \quad \gamma(h) = \frac{1}{2n} \sum_{i=1}^n (z(s_i) - z(s_i + h))^2 \quad (4)$$

231 where n is the number of data pairs with the attribute z separated by distance h .

232 To obtain the semivariogram at any h , a theoretical semivariogram model should be fitted to the
233 experimental values. There are four commonly used theoretical semivariogram models: the spherical,
234 Gaussian, exponential, and power models. The best one with the highest fitting R^2 was used in the
235 study.

236 3.3. Working procedure of the proposed method

237 The detailed steps of SRF-DC are as follows (Fig. 3):

238 (1) Each pixel value of the 10 km IMERG was re-estimated by OK interpolation with its k nearest
239 neighbors (e.g. $k=8$) to obtain the interpolated IMERG (termed as $I_s^{10\text{km}}$), the 10 km IMERG
240 was interpolated by OK to obtain the interpolated 1 km IMERG ($I_s^{1\text{km}}$), and the gauge
241 observations were interpolated by OK to produce the 1 km precipitation map ($P_s^{1\text{km}}$). This step
242 aims to provide spatial variables for SRF, i.e. X_s in Eq. (1). Since the semivariogram model cannot
243 be accurately estimated from the sparse gauge measurements, the satellite-based precipitation was
244 used to derive the model, as suggested by Chen et al. (2020c). To estimate $I_s^{10\text{km}}$ and $I_s^{1\text{km}}$, the
245 raster-based 10 km IMERG was first transformed into the point-based form with spatial
246 coordinates and precipitation values, and then the scattered points were interpolated by OK to
247 produce raster-based maps.

248 (2) The negative NDVI values were excluded from the original data, which mainly belong to snow
249 and water bodies in the study site. The removed values were interpolated by OK with their
250 neighbors to avoid information loss.

251 (3) The 1 km environmental variables $\mathbf{X}_{ns}^{1\text{km}}$ (i.e. NDVI, LST_D, LST_N, LST_{D-N}, DEM, slope, aspect,
252 terrain relief, latitude and longitude) were resampled to the 10 km resolution $\mathbf{X}_{ns}^{10\text{km}}$ by the pixel
253 averaging method because the average value reflects the overall trend within each 10 km pixel and
254 reduces the influence of outliers in the 1 km pixels.

255 (4) The relationship between $\mathbf{X}_{ns}^{10\text{km}}$, $I_s^{10\text{km}}$ and the original 10 km IMERG ($D^{10\text{km}}$) was
256 constructed by SRF:

$$257 \quad D^{10\text{km}}(s_0) = f_{\text{downscale}}(I_s^{10\text{km}}(s_0), \mathbf{X}_{ns}^{10\text{km}}(s_0)) + e^{10\text{km}}(s_0) \quad (5)$$

258 where e is the fitting residual.

259 (5) The 10 km IMERG ($D^{10\text{km}}$) was downscaled to 1 km ($D^{1\text{km}}$) by applying the constructed model
260 in step (4) to $\mathbf{X}_{ns}^{1\text{km}}$ and $I_s^{1\text{km}}$:

$$261 \quad D^{1\text{km}} = f_{\text{downscale}}(I_s^{1\text{km}}, \mathbf{X}_{ns}^{1\text{km}}) \quad (6)$$

262 (6) The relationship between the 1 km predictors and the gauge observations (G) was constructed by

263 SRF:

$$264 \quad G(s_0) = f_{\text{calibrate}}(P_s^{1\text{km}}(s_0), D^{1\text{km}}(s_0), \mathbf{X}_{ns}^{1\text{km}}(s_0)) + e^{1\text{km}}(s_0) \quad (7)$$

265 (7) The 1 km precipitation data ($C^{1\text{km}}$) was produced based on the constructed relationship in step

266 (6):

$$267 \quad C^{1\text{km}} = f_{\text{calibrate}}(P_s^{1\text{km}}, D^{1\text{km}}, \mathbf{X}_{ns}^{1\text{km}}) \quad (8)$$

268 In this study, residual correction was ignored during downscaling and calibration, as many previous
269 studies (Karbalye Ghorbanpour et al., 2021; Lu et al., 2019) demonstrated that residual correction on
270 the ML-based technique could decrease prediction accuracy.

271 3.4. Comparative methods

272 In the study, the performance of SRF-DC was comparatively assessed under three manners. Firstly,
273 we compared the results of SRF-DC with those of the classical methods including GWR, RF and
274 BPNN. Secondly, SRF-DC was compared with two frameworks: (i) the IMERG was first downscaled
275 by the bilinear interpolation and then calibrated by SRF (termed as Bi-SRF), and (ii) the IMERG was
276 first downscaled by SRF and then calibrated by GDA (termed as SRF-GDA). Thirdly, SRF-DC at the
277 monthly scale was compared with the annual-based SRF fraction disaggregation method (termed as
278 SRFdis). Specifically, the IMMERG was first downscaled and calibrated by SRF on an annual scale
279 and then the estimated annual precipitation was disaggregated into monthly precipitation using monthly
280 fractions, as proposed by Duan and Bastiaanssen (2013). Finally, SRF-DC was compared with OK
281 interpolation only on gauge measurements (termed as kriging). Overall, SRF-DC was compared with
282 seven classical methods in this study including GWR, RF, BPNN, Bi-SRF, SRF-GDA, SRFdis and
283 kriging.

284 To quantitatively analyze the performance of all the methods, all rain gauge observations were
285 randomly divided into l folds (e.g. $l=10$), where the $l-1$ folds (i.e. training/validating data) was used to
286 construct the model, while the remaining fold (i.e. testing data) to assess the performance of the model
287 (Xu and Goodacre, 2018). During model construction, the $l-1$ folds were randomly divided into training
288 and validating datasets with the proportions of 80% and 20%, respectively, where the former was used
289 to train the model and the latter to validate the model. Then, the performance of the model with the

290 optimized parameters was assessed using the testing data. The aforementioned process was repeated l
 291 times until all folds were taken as the testing data.

292 3.5. Accuracy measures

293 We comparatively analyzed the performance of all methods with four accuracy measures including
 294 root mean square error (RMSE), mean error (ME), mean absolute error (MAE) and correlation
 295 coefficient (CC) (Jing et al., 2016; Sharifi et al., 2019). They are respectively expressed as follows:

$$296 \quad RMSE = \sqrt{\frac{1}{n} \sum_{i=1}^n (E_i - O_i)^2} \quad (9)$$

$$297 \quad ME = \frac{\sum_{i=1}^n (E_i - O_i)}{n} \quad (10)$$

$$298 \quad MAE = \frac{\sum_{i=1}^n |E_i - O_i|}{n} \quad (11)$$

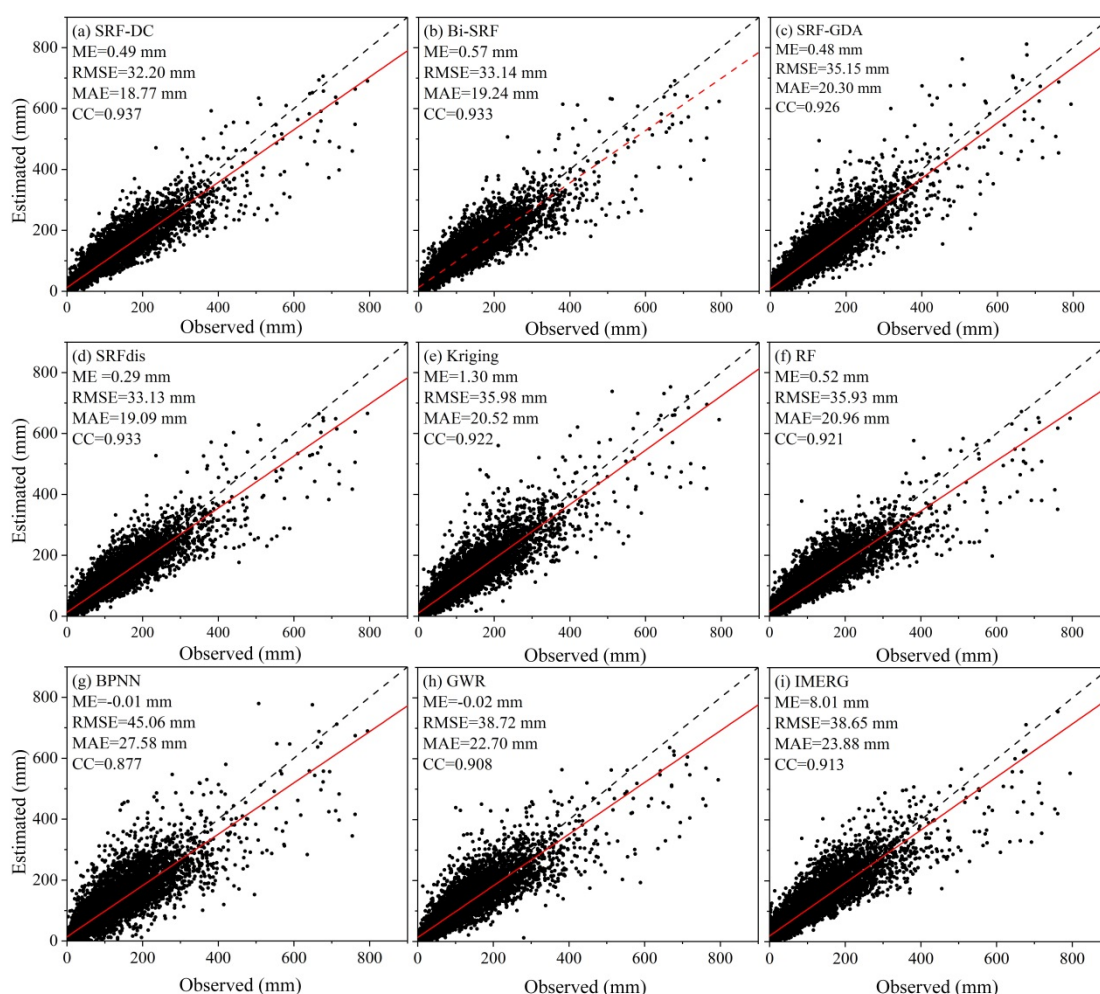
$$299 \quad CC = \frac{\sum_{i=1}^n (E_i - \bar{E})(O_i - \bar{O})}{\sqrt{\sum_{i=1}^n (E_i - \bar{E})^2} \times \sqrt{\sum_{i=1}^n (O_i - \bar{O})^2}} \quad (12)$$

300 where n is the number of testing points, and E_i and O_i are the estimated and observed precipitation at
 301 location i , respectively.

302 4. Results and analysis

303 Fig. 5 illustrates the scatterplots between the predicted and observed precipitation on a monthly scale
 304 from 2015 to 2019. Results show that the original IMMERG is heavily biased with the ME value of
 305 8.01 mm. In contrast, except for kriging, all the other models greatly reduce the bias with the ME
 306 values approximate to zero. In other words, the models with the incorporation of high resolution
 307 variables become unbiased. With respect to RMSE, MAE and CC, BPNN produces worse results than
 308 the original IMMERG. The performance of GWR is also unsatisfactory. This is mainly attributed to the
 309 complex relationship between precipitation and predictors, which cannot be properly described by the

310 two models. RF and kriging perform better than IMERG. The four SRF-based methods including
 311 SRF-DC, Bi-SRF, SRF-GDA and SRFdis outperform the other methods. This indicates the importance
 312 of spatial autocorrelation for precipitation estimation. Moreover, among the four versions of SRF,
 313 SRF-GDA has the lowest accuracy, indicating that SRF is more important for calibration than
 314 downscaling. SRF-DC with the RMSE, MAE and CC values of 32.20 mm, 18.77 mm and 0.937
 315 produces the best result. Thus, it can be concluded that (i) SRF-based downscaling and calibration is
 316 more effective than bilinear downscaling (Bi-SRF) and GDA-based calibration (SRF-GDA) and (ii)
 317 there is no obvious time latency for vegetation response to precipitation in the study site, as SRF-DC
 318 on the monthly scale is slightly more accurate than SRFdis on the annual scale.



319
 320 Fig. 5 Scatterplots between the estimated and observed precipitation on a monthly scale from 2015 to
 321 2019 (fitting line with the red color models the relationship between the observed and estimated
 322 precipitation)

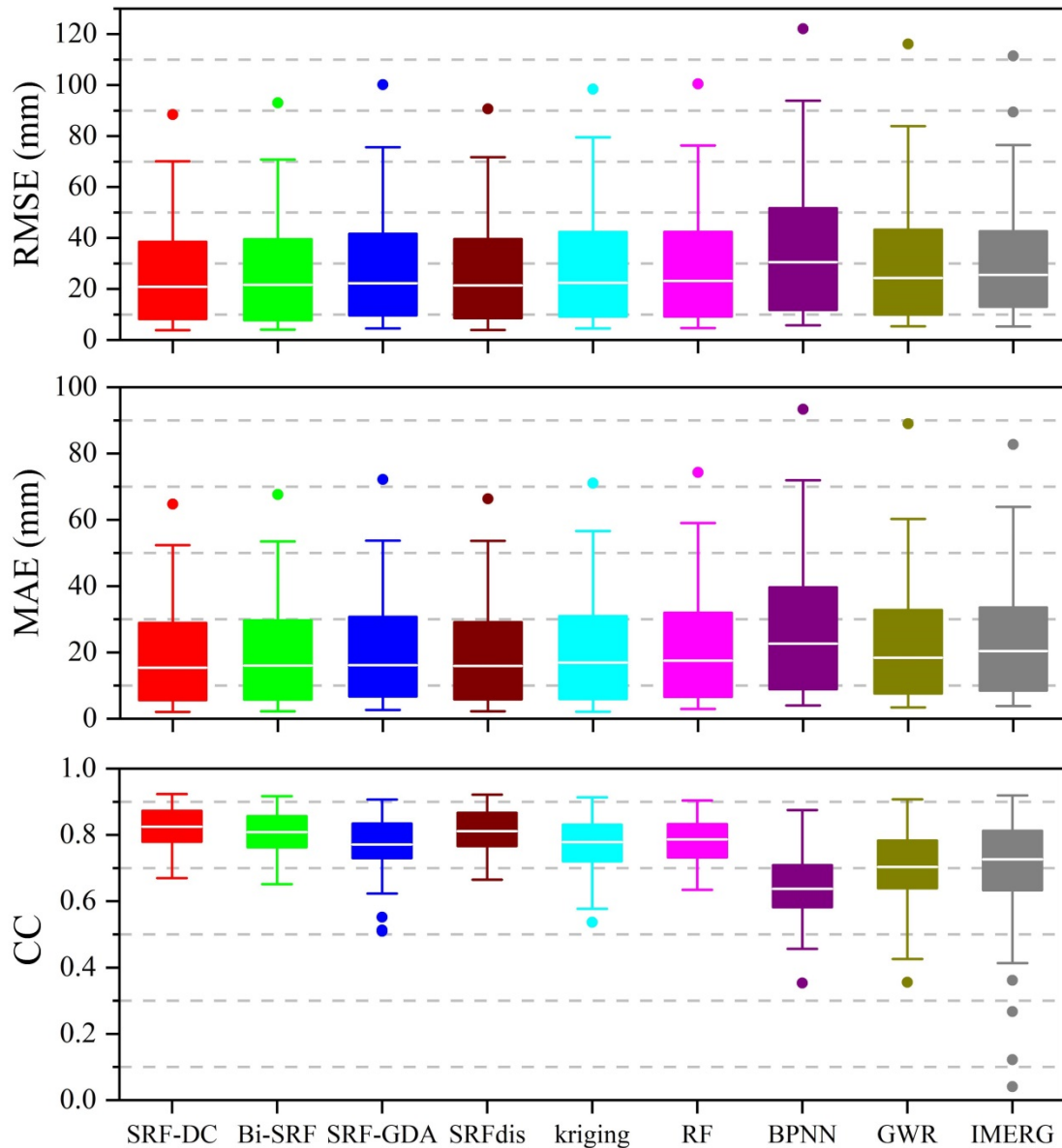
323 However, as shown in Fig. 5, all the methods significantly underestimate precipitation when the

324 values are greater than 400 mm. To quantitatively analyze the performance of all methods on the high
 325 precipitation, their accuracy measures are shown in Table 2. Results show that all methods have poor
 326 results for these observations. A possible reason is that high precipitation is often caused by
 327 complicated environmental factors, which cannot be sufficiently explained by the constructed
 328 predictors-precipitation relationships. In terms of ME, SRF-GDA ranks the first, which is followed by
 329 kriging and SRF-DC. However, their ME values are less than -70 mm. With respect to RMSE and
 330 MAE, kriging performs the best, which is closely followed by SRF-DC, while with respect to CC,
 331 SRF-DC with the value of 0.64 outperforms the others.

332 Table 2 Accuracy measures of all methods for estimating high precipitation (i.e. values greater than 400
 333 mm)

Method	ME (mm)	RMSE (mm)	MAE (mm)	CC
SRF-DC	-105.54	149.80	124.82	0.64
Bi-SRF	-110.96	156.81	130.67	0.60
SRF-GDA	-74.21	150.10	126.02	0.55
SRFdis	-117.31	160.11	137.29	0.61
Kriging	-86.25	146.94	119.53	0.58
RF	-141.53	177.71	150.83	0.61
BPNN	-118.88	171.23	142.00	0.57
GWR	-139.02	178.85	145.19	0.57
IMERG	-136.22	173.24	143.69	0.55

334 Fig. 6 shows the boxplots of the four accuracy measures. Obviously, BPNN obtains the lowest
 335 accuracy. It is followed by GWR and IMERG. RF and kriging show better results than BPNN, GWR
 336 and IMERG. The four methods based on SRF seem more accurate than the classical methods.
 337 Moreover, SRF-DC slightly outperforms the other SRF-based methods, which highlights the benefit of
 338 including spatial autocorrelation for downscaling and calibration of satellite-based precipitation.



339

340

341

342

343

344

345

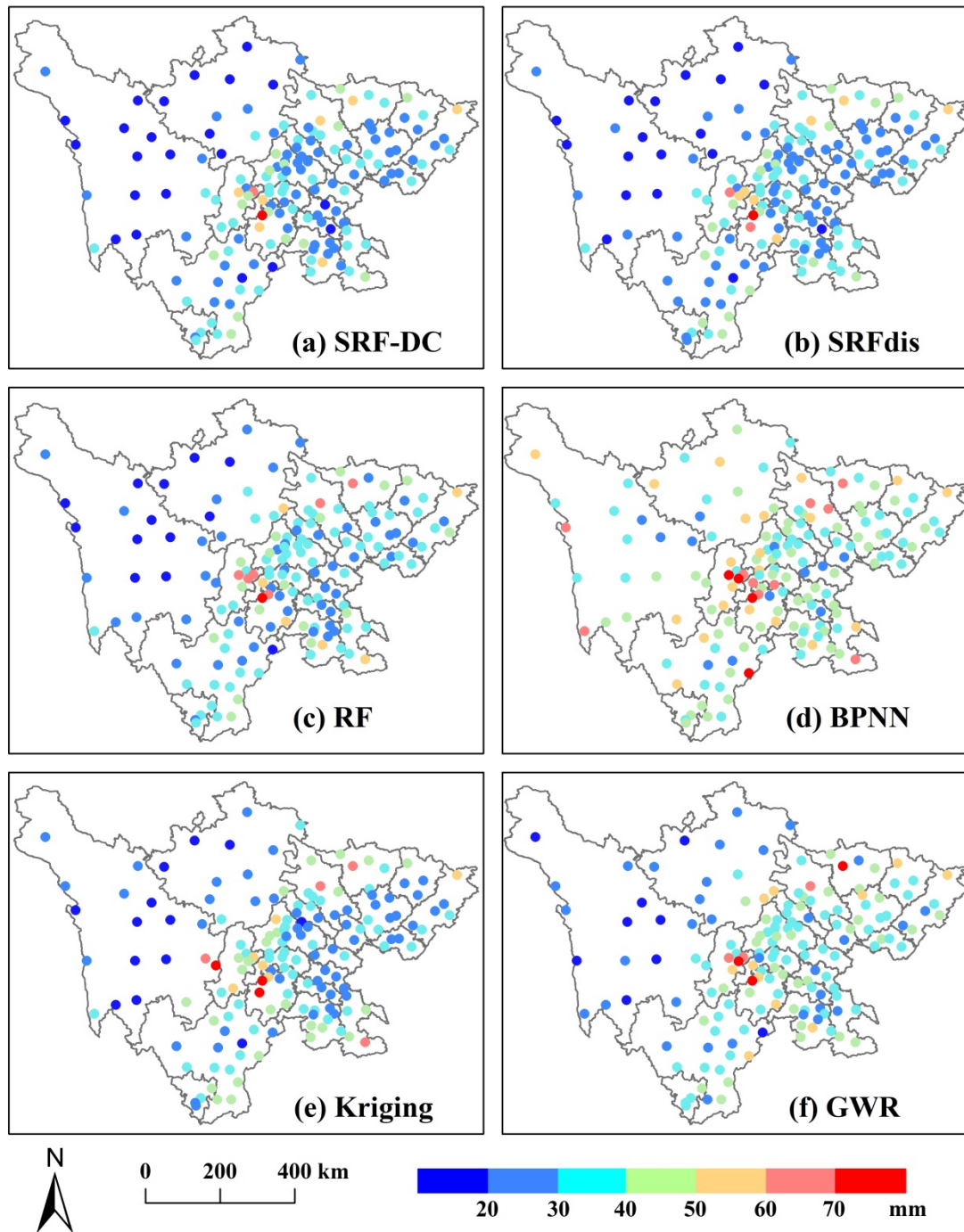
346

347

Fig. 6 Boxplots of RMSE, MAE and CC values of all the methods on a monthly scale during

2015-2019

Fig. 7 shows the RMSE spatial distributions of SRF-DC, SRFdis, RF, BPNN, kriging and GWR on all gauge stations. Overall, the RMSEs tend to be larger in the middle area, since it has higher precipitation than the other areas (Fig. 1). BPNN (Fig. 7d) yields the poorest result, where many stations have the RMSE values greater than 60 mm. It is followed by GWR (Fig. 7f). RF (Fig. 7c) and kriging (Fig. 7e) are better than GWR and BPNN at most stations. SRF-DC (Fig. 7a) and SRFdis (Fig. 7b) are more accurate than the classical methods, especially at the stations in the middle area.

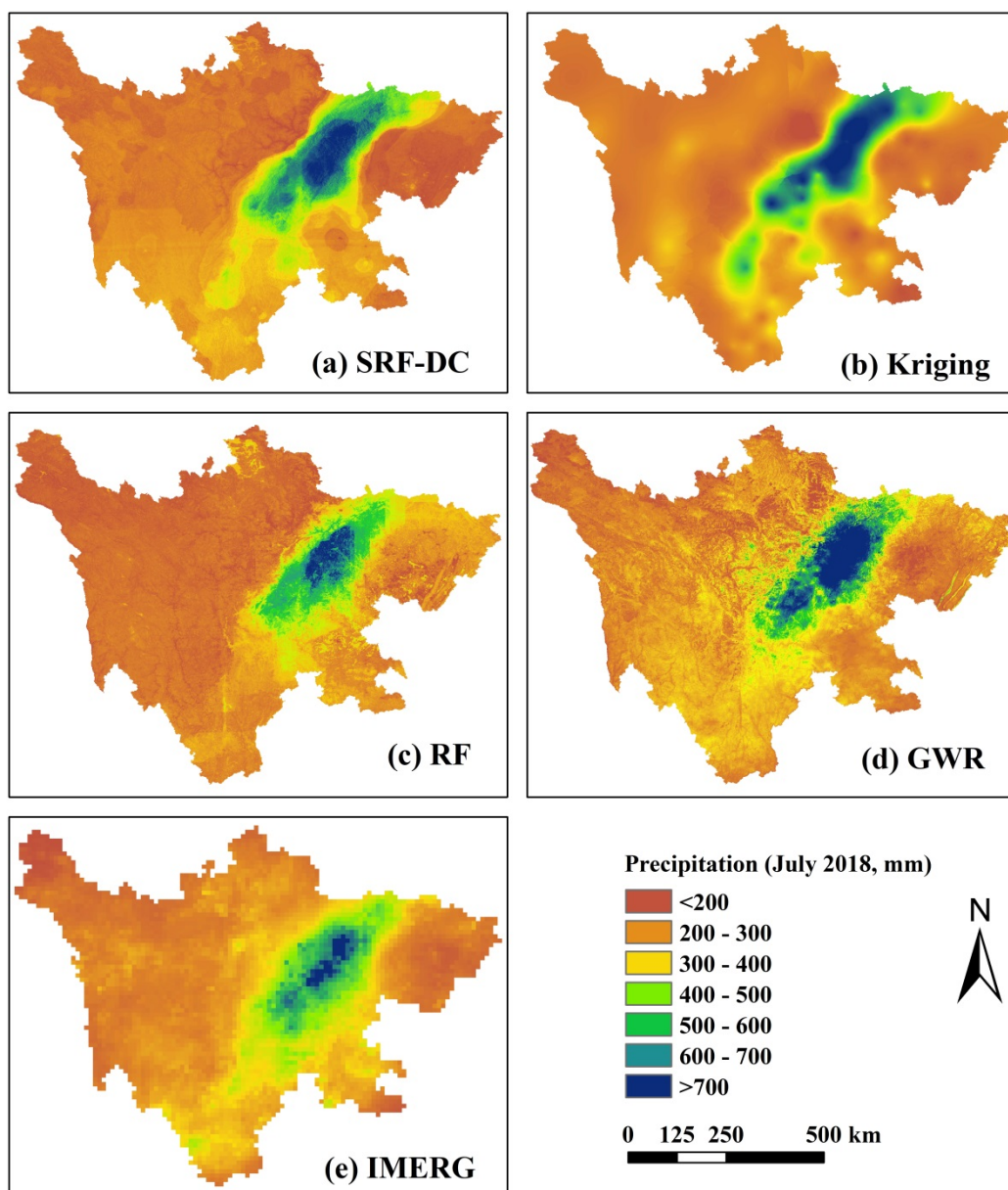


348

349 Fig. 7 RMSE distributions of SRF-DC and some representative methods for all gauge stations on a
 350 monthly scale during 2015-2019

351 Since the wettest month is July 2018 (Fig. 2), it is taken as an example to show the precipitation
 352 maps of SRF-DC and some classical methods. Moreover, the semivariogram of kriging derived from
 353 the original IMMERG and its prediction error map are shown, since they play an important role in the
 354 performance of kriging and SRF-based methods. Results (Fig. 8) indicate that precipitation produced
 355 by all the methods have spatial distribution patterns similar to IMERG, with much high precipitation in

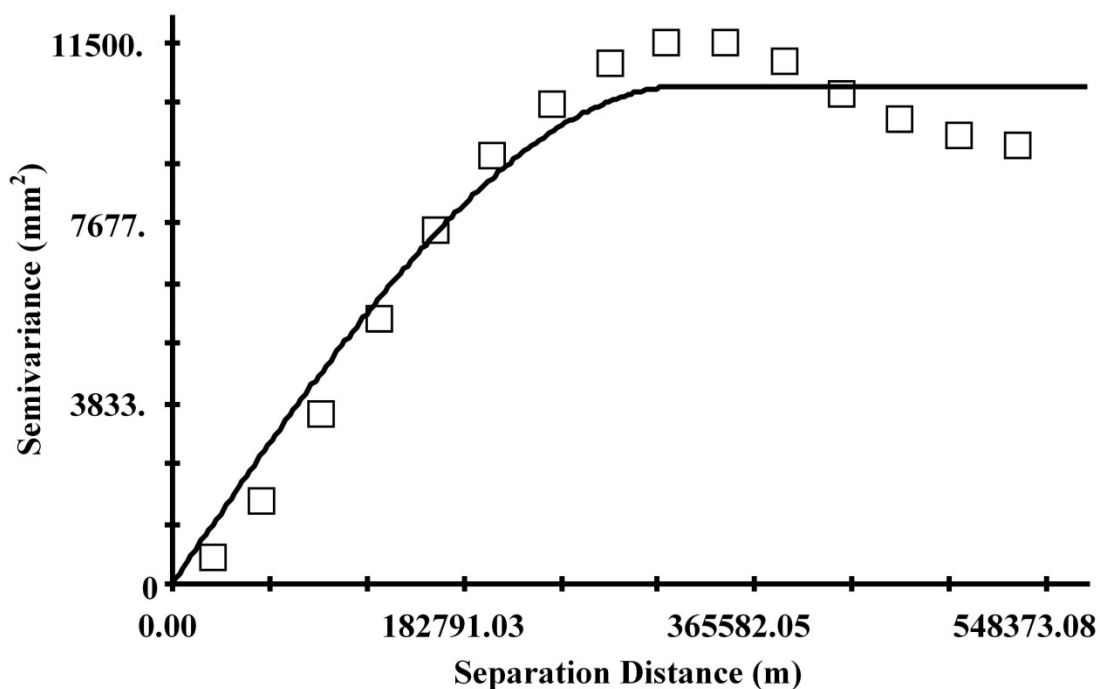
356 the middle and low precipitation in the east. The ML-based methods have more spatial details of
 357 precipitation than IMERG due to the inclusion of high-resolution predictors for precipitation estimation.
 358 The kriging map is so smooth that many details and variations of precipitation pattern are lost. This is
 359 expected as it only uses ground measurements for the interpolation. RF shows obvious unnatural
 360 discontinuities at the bottom. GWR suffers from systematic anomalies, with the values clearly greater
 361 than their neighbors. In comparison, SRF-DC produces a good precipitation map.



362
 363 Fig. 8 Downscaled and calibrated precipitation maps of SRF-DC and some representative methods on
 364 the wettest month (July 2018)

365 The semivariogram and prediction error map of OK are shown in Fig. 9. Obviously, OK has a

366 spherical model with the nugget variance (C_0) of 10.0 m^2 , sill (C_0+C) of 10,560 m^2 , residual sum of
 367 squares (Rss) of 8,800,611 m^2 , range (A_0) of 321,000 m, and fitting R^2 of 0.962, respectively (Fig. 9a).
 368 The prediction error map (Fig. 9b) illustrates that the errors in the west are larger than in the east, and
 369 in the boundary are larger than in the inner. It can be inferred that large errors are mainly located in the
 370 areas with the sparse distribution of rain gauges. Moreover, the error magnitudes are not related to
 371 RMSE distribution (Fig. 7) and precipitation pattern (Fig. 8).



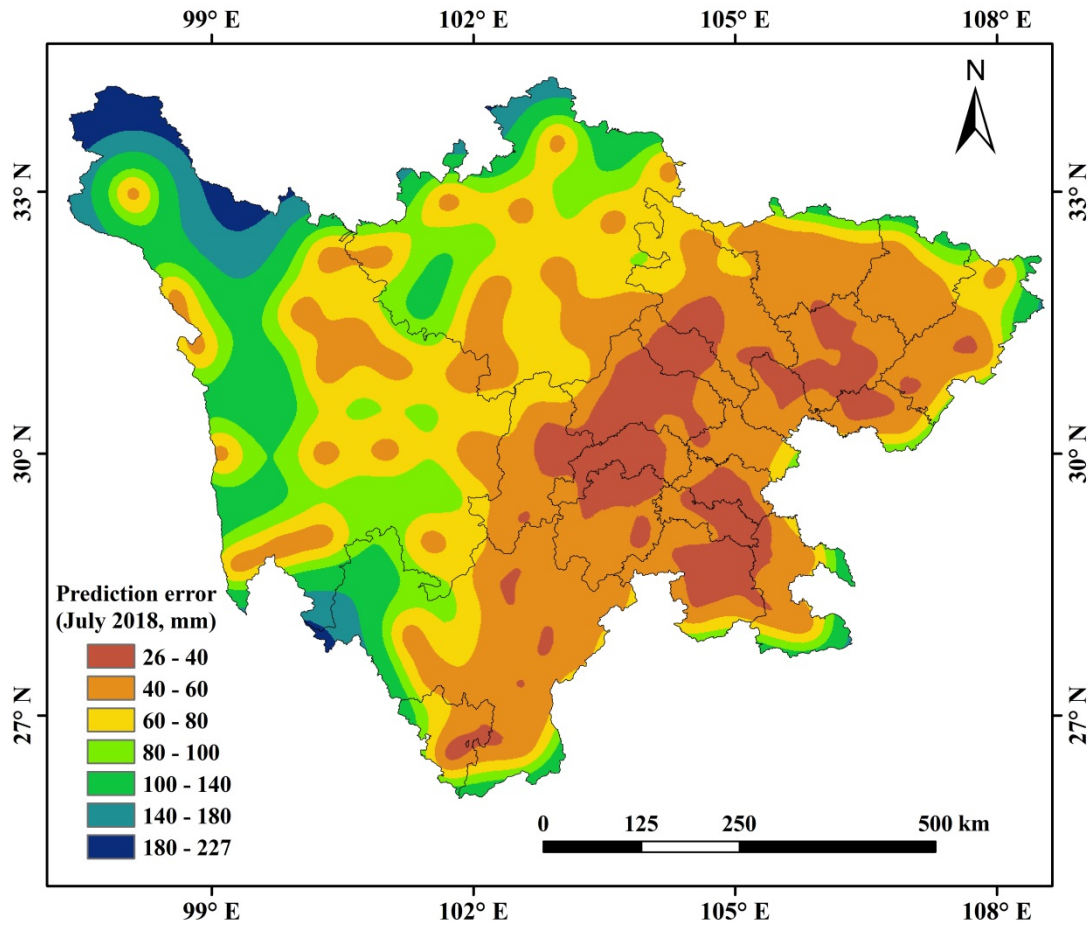
**Spherical model ($C_0 = 10.0$; $C_0 + C = 10560.0$; $A_0 = 321000.0$; $r^2 = 0.962$;
Rss = 8800611.)**

372

373

(a) Semivariogram

374



(b) Prediction error

Fig. 9 Semivariogram and prediction error map of kriging on the wettest month (July 2018)

5. Discussion

For downscaling and calibration of satellite-based precipitation, the three most important factors for constructing predictors-precipitation relationships are model, predictor and temporal scale (Chen et al., 2020b). Thus, they should be carefully selected to produce accurate precipitation data.

5.1. Model

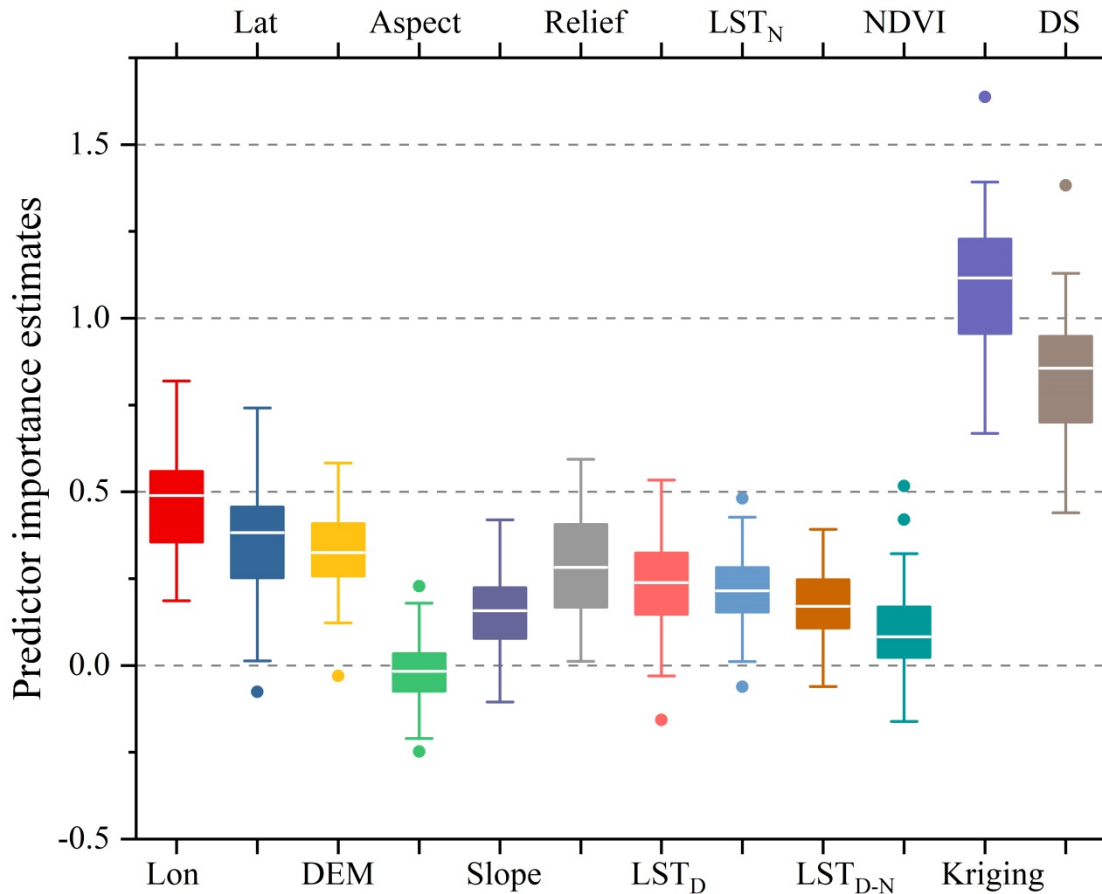
In previous studies, the most commonly adopted model was GWR (Xu et al., 2015; Chen et al., 2015; Zhao et al., 2018), since it considers the spatial variation between the predictors and precipitation. However, due to the sparse distribution of rain gauge stations (Lu et al., 2019), GWR produced worse results than the original IMERG in the study region. RF and kriging outperformed GWR. Nevertheless,

387 the two methods have some shortcomings. For example, the precipitation map of kriging was so
388 smooth that many details were lost, and RF did not consider the spatial autocorrelation of precipitation
389 measurements. In comparison, SRF-based methods with the consideration of spatial autocorrelation
390 information demonstrated higher accuracy than the classical methods. Moreover, SRF-DC yielded
391 slightly better results than Bi-SRF, SRF-GDA and SRFdis.

392 **5.2. Environmental predictors**

393 NDVI, latitude, longitude and DEM-based parameters were commonly adopted as predictors to
394 estimate precipitation (Shi et al., 2015). However, satellite-based precipitation across regions with no
395 relationship with NDVI could not be estimated, such as in barren or snow areas (Xu et al., 2015). Jing
396 et al. (2016) indicated that the downscaled models including LST features (LSTs) performed better
397 than those without LSTs. Thus, in addition to NDVI and DEM-related parameters, daytime LST
398 (LST_D), nighttime LST (LST_N), and difference between day and night LSTs (LST_{D-N}) were used in
399 this study.

400 Based on RF, the relative importance of each predictor (i.e. predictor importance estimate) is shown
401 in Fig. 10. Obviously, precipitation from kriging interpolation has the most importance. This is
402 because the interpolated value is directly related to precipitation. Kriging estimation is followed by
403 the downscaled precipitation. Longitude is the third most important variable, which is followed by
404 latitude. This result is consistent with that of Karbalaye Ghorbanpour et al. (2021). They indicated
405 that compared to NDVI, LST and DEM, longitude ranks the first with respect to importance score.



406

407 Fig. 10 Predictor importance estimates (Lat: latitude; Lon: longitude; DS: downscaled precipitation)

408 The three LSTs also have a great impact on the precipitation estimation, where LST_D seems slightly
 409 more important than LST_N and LST_{D-N}. NDVI has a slight effect on the precipitation, which ranks last
 410 but one. This might be due to the fact that NDVI is influenced by both precipitation and temperature
 411 in the study site, and the low temperature above certain elevations hinders the vegetation growth. It is
 412 less likely that the response of vegetation to precipitation has the delay, since SRF-DC on the monthly
 413 scale is more accurate than SRFdis on the annual scale.

414 Among the 12 predictors, aspect has the least importance. This conclusion was also obtained by Ma
 415 et al. (2017) for downscaling TMPA 3B43 V7 data over the Tibet Plateau. DEM, terrain relief and
 416 slope seem more important than aspect, since precipitation is closely related to topography (Jing et al.,
 417 2016). The results are consistent with previous studies (Immerzeel et al., 2009; Jing et al., 2016).

418 **5.3. Temporal scale**

419 Temporal scale has a great effect on the selection of predictors for precipitation estimation. There is a

420 debate on whether NDVI should be taken as a predictor for downscaling and calibration of monthly
421 precipitation. Some (Duan and Bastiaanssen, 2013; Immerzeel et al., 2009) argued that NDVI could not
422 be used for monthly precipitation estimation since the response of NDVI to precipitation usually
423 delayed for two or three months. However, some (Brunsell, 2006; Xu et al., 2015; Lu et al., 2019; Chen
424 et al., 2020c) stated that the precipitation-NDVI relationship was hardly time-delayed, since vegetation
425 could influence precipitation by adjusting temperature and air moisture during the growing seasons.
426 Thus, it was possible to estimate precipitation with NDVI at the monthly scale. In this study, it was
427 found that SRF-DC on the monthly scale was slightly more accurate than that on the annual scale (i.e.
428 SRFdis). This indicates that the response of vegetation to precipitation has no obvious time delay, and
429 NDVI can be used for monthly precipitation estimates.

430 **5.4. Easy-to-use feature**

431 Since the classical RF did not consider the spatial information in the modeling process, Hengl et al.
432 (2018) proposed an improved RF for spatial estimation, where the buffer distances between the
433 estimated location and measured locations were taken as the predictors. Motivated by this idea,
434 Baez-Villanueva et al. (2020) presented a RF-based method (RF-MEP) for merging satellite
435 precipitation products and rain gauge measurements, where the spatial distances from all rain gauges to
436 the grid cells in the study site were used as the variables. However, as stated by Baez-Villanueva et al.
437 (2020), RF-MEP has a huge computational cost, since the number of extra input features equals to that
438 of gauge measurements. Moreover, RF-MEP ignores the spatial autocorrelation of precipitation
439 between neighboring locations. In comparison, SRF only requires one extra feature that is estimated by
440 kriging interpolation on the precipitation measurements. Thus, compared to the buffer distance
441 layers-based RF, SRF is highly effective. Moreover, with the variogram-based kriging interpolation, the
442 spatial autocorrelation of precipitation not only between the gauge locations, but also between the
443 estimated location and gauge locations is taken into account. Thus, SRF has the merits of accuracy,
444 effectivity and ease of use.

445 **5.5. Limitations and further researches**

446 Although SRF-DC shows promising results than the classical methods, it still suffers from some

447 limitations, which should be solved in our further researches. Firstly, SRF-DC is more complex than
448 Bi-SRF and SRF-GDA, since SRF is used in both downscaling and calibration. Applying SRF to
449 downscale IMMERG might not be prerequisite since SRF-DC is only slightly better than Bi-SRF.
450 However, SRF should be used to calibrate IMMERG due to the much higher accuracy of SRF-DC than
451 SRF-GDA. Secondly, SRF-DC has low accuracy on high precipitation (e.g. >400 mm) since extreme
452 precipitation is often caused by unpredictable factors. Thus, other available variables such as soil
453 moisture (Fan et al., 2019; Brocca et al., 2019), and meteorological conditions such as cloud properties
454 (Sharifi et al., 2019) could be adopted to further improve IMMERG quality. Thirdly, the correction of
455 satellite-based precipitation on higher-temporal scales (e.g. daily or hourly) is challenging and valuable
456 (Wu et al., 2020; Chen et al., 2020b; R. Lima et al., 2021; Sun and Lan, 2021). Although SRF-DC is
457 general, its performance on these scales should be further assessed. Finally, numerous satellite-based
458 precipitation products have been available, and each one has its shortcomings and advantages for the
459 capture of spatial precipitation patterns (Chen et al., 2020c; Baez-Villanueva et al., 2020). Thus, the
460 fusion of multiple precipitation products based on SRF-DC is an alternative to improve the quality of
461 precipitation data.

462 **6. Conclusions**

463 To enhance the resolution (from 0.1° to 1 km) and accuracy of the monthly IMERG V06B Final Run
464 product, a spatial RF (SRF)-based downscaling and calibration method (SRF-DC) was proposed in this
465 study. The performance of SRF-DC was compared with those of seven methods including GWR, RF,
466 BPNN, Bi-SRF, SRF-GDA, SRFdis and kriging on monthly IMERG from 2015 to 2019 over Sichuan
467 province, China. The main findings and conclusions can be summarized as follows:

- 468 (1) The SRF-based methods including SRF-DC, Bi-SRF, SRF-GDA and SRFdis were more accurate
469 than the classical methods. Moreover, SRF-DC performed slightly better than Bi-SRF and
470 SRF-GDA.
- 471 (2) The comparison between the monthly-based and annual-based estimation demonstrated that there
472 was no statistically significant difference between them, indicating that NDVI could be used for
473 monthly precipitation estimation in the study site.
- 474 (3) Kriging outperformed the original IMERG, BPNN and GWR in terms of RMSE, MAE and CC.

475 However, its interpolation map suffered from the serious loss of spatial precipitation patterns.
476 (4) Based on the variable importance assessment of RF, the precipitation interpolated by kriging on the
477 gauge measurements was the most important variable, while terrain aspect was the least one. This
478 indicated that considering spatial correlation was beneficial for precipitation estimation.
479 Overall, SRF-DC is general, robust, accurate and easy-to-use, as it shows promising results in the
480 study area with heterogeneous terrain morphology and precipitation. Thus, it can be easily applied to
481 other regions, where precipitation data with high resolution and high accuracy is urgently required.

482 **Data availability**

483 The gauge data are from the China Meteorological Data Service Center (<http://data.cma.cn>, last
484 access: January 2021). The GPM data are from <https://gpm.nasa.gov/data> (last access: January 2021).
485 The GPM data are from <http://srtm.csi.cgiar.org/> (last access: January 2021). The MOD13A3 data are
486 from <http://www.gscloud.cn/> (last access: January 2021). The MOD11A2 data are from
487 <https://ladsweb.modaps.eosdis.nasa.gov> (last access: January 2021).

488 **Declaration of Competing Interest**

489 The authors declare that they have no known competing financial interests or personal relationships
490 that could have appeared to influence the work reported in this paper.

491 **Author contributions**

492 CF and YY conceived the idea, and acquired the project and financial support. BJ conducted the
493 detailed analysis. CF contributed to the writing and revisions.

494 **Competing interests**

495 The authors declare that they have no conflict of interest.

496 **Acknowledgement**

497 This work was supported by the National Natural Science Foundation of China (Grant No.
498 41804001), Shandong Provincial Natural Science Foundation, China (Grant No. ZR2020YQ26,
499 ZR2019MD007, ZR2019BD006), A Project of Shandong Province Higher Educational Youth

500 Innovation Science and Technology Program (Grant No. 2019KJH007), Shandong Provincial Key
501 Research and Development Program (Major Scientific and Technological Innovation Project) (Grant
502 No. 2019JZZY010429) and by the Scientific Research Foundation of Shandong University of Science
503 and Technology for Recruited Talents (Grant No. 2019RCJJ003).

504

References

- 505 Ashouri, H., Hsu, K.-L., Sorooshian, S., Braithwaite, D. K., Knapp, K. R., Cecil, L. D., Nelson, B. R.,
506 and Prat, O. P.: PERSIANN-CDR: Daily Precipitation Climate Data Record from Multisatellite
507 Observations for Hydrological and Climate Studies, *Bulletin of the American Meteorological*
508 *Society*, 96, 69-83, 10.1175/bams-d-13-00068.1, 2015.
- 509 Baez-Villanueva, O. M., Zambrano-Bigiarini, M., Beck, H. E., McNamara, I., Ribbe, L., Nauditt, A.,
510 Birkel, C., Verbist, K., Giraldo-Osorio, J. D., and Xuan Thinh, N.: RF-MEP: A novel Random
511 Forest method for merging gridded precipitation products and ground-based measurements,
512 *Remote Sensing of Environment*, 239, 111606, <https://doi.org/10.1016/j.rse.2019.111606>, 2020.
- 513 Beck, H. E., van Dijk, A. I. J. M., Levizzani, V., Schellekens, J., Miralles, D. G., Martens, B., and de
514 Roo, A.: MSWEP: 3-hourly 0.25° global gridded precipitation (1979–2015) by merging gauge,
515 satellite, and reanalysis data, *Hydrology and Earth System Sciences*, 21, 589-615,
516 10.5194/hess-21-589-2017, 2017.
- 517 Beck, H. E., Wood, E. F., Pan, M., Fisher, C. K., Miralles, D. G., van Dijk, A. I. J. M., McVicar, T. R.,
518 and Adler, R. F.: MSWEP V2 Global 3-Hourly 0.1° Precipitation: Methodology and Quantitative
519 Assessment, *Bulletin of the American Meteorological Society*, 100, 473-500,
520 10.1175/bams-d-17-0138.1, 2019.
- 521 Belgiu, M., Drăguț, L. J. I. J. o. P., and Sensing, R.: Random forest in remote sensing: A review of
522 applications and future directions, 114, 24-31, 2016.
- 523 Berndt, C. and Haberlandt, U.: Spatial interpolation of climate variables in Northern
524 Germany-Influence of temporal resolution and network density, *Journal of Hydrology-Regional*
525 *Studies*, 15, 184-202, 10.1016/j.ejrh.2018.02.002, 2018.
- 526 Berndt, C., Rabiei, E., and Haberlandt, U.: Geostatistical merging of rain gauge and radar data for high
527 temporal resolutions and various station density scenarios, *Journal of Hydrology*, 508, 88-101,
528 <https://doi.org/10.1016/j.jhydrol.2013.10.028>, 2014.
- 529 Bhuiyan, M. A. E., Nikolopoulos, E. I., Anagnostou, E. N., Quintana-Seguí, P., and Barella-Ortiz, A.:
530 A nonparametric statistical technique for combining global precipitation datasets: development and
531 hydrological evaluation over the Iberian Peninsula, *Hydrology and Earth System Sciences*, 22,
532 1371-1389, 10.5194/hess-22-1371-2018, 2018.
- 533 Breiman, L.: Random Forests, *Machine Learning*, 45, 5-32, 2001.
- 534 Brocca, L., Filippucci, P., Hahn, S., Ciabatta, L., Massari, C., Camici, S., Schüller, L., Bojkov, B., and
535 Wagner, W.: SM2RAIN–ASCAT (2007–2018): global daily satellite rainfall data from ASCAT soil
536 moisture observations, *Earth System Science Data*, 11, 1583-1601, 10.5194/essd-11-1583-2019,
537 2019.
- 538 Brunsell, N. A.: Characterization of land-surface precipitation feedback regimes with remote sensing,
539 *Remote Sensing of Environment*, 100, 200-211, <https://doi.org/10.1016/j.rse.2005.10.025>, 2006.
- 540 Chao, L., Zhang, K., Li, Z., Zhu, Y., Wang, J., and Yu, Z.: Geographically weighted regression based
541 methods for merging satellite and gauge precipitation, *Journal of Hydrology*, 558, 275-289,

542 <https://doi.org/10.1016/j.jhydrol.2018.01.042>, 2018.

543 Cheema, M. J. M. and Bastiaanssen, W. G. M.: Local calibration of remotely sensed rainfall from the
544 TRMM satellite for different periods and spatial scales in the Indus Basin, *International Journal of*
545 *Remote Sensing*, 33, 2603-2627, 10.1080/01431161.2011.617397, 2012.

546 Chen, C., Yang, S., and Li, Y.: Accuracy Assessment and Correction of SRTM DEM using
547 ICESat/GLAS Data under Data Coregistration, *Remote Sensing*, 12, 3435, 10.3390/rs12203435,
548 2020a.

549 Chen, C., Zhao, S., Duan, Z., and Qin, Z.: An Improved Spatial Downscaling Procedure for TRMM
550 3B43 Precipitation Product Using Geographically Weighted Regression, *IEEE Journal of Selected*
551 *Topics in Applied Earth Observations and Remote Sensing*, 8, 4592-4604,
552 10.1109/JSTARS.2015.2441734, 2015.

553 Chen, F., Gao, Y., Wang, Y., and Li, X.: A downscaling-merging method for high-resolution daily
554 precipitation estimation, *Journal of Hydrology*, 581, 124414,
555 <https://doi.org/10.1016/j.jhydrol.2019.124414>, 2020b.

556 Chen, F., Liu, Y., Liu, Q., and Li, X.: Spatial downscaling of TRMM 3B43 precipitation considering
557 spatial heterogeneity, *International Journal of Remote Sensing*, 35, 3074-3093,
558 10.1080/01431161.2014.902550, 2014.

559 Chen, J., Brissette, F. P., Chaumont, D., and Braun, M.: Finding appropriate bias correction methods in
560 downscaling precipitation for hydrologic impact studies over North America, *Water Resources*
561 *Research*, 49, 4187-4205, <https://doi.org/10.1002/wrcr.20331>, 2013.

562 Chen, S.-T., Yu, P.-S., and Tang, Y.-H.: Statistical downscaling of daily precipitation using support
563 vector machines and multivariate analysis, *Journal of Hydrology*, 385, 13-22,
564 <https://doi.org/10.1016/j.jhydrol.2010.01.021>, 2010.

565 Chen, S., Xiong, L., Ma, Q., Kim, J.-S., Chen, J., and Xu, C.-Y.: Improving daily spatial precipitation
566 estimates by merging gauge observation with multiple satellite-based precipitation products based
567 on the geographically weighted ridge regression method, *Journal of Hydrology*, 589, 125156,
568 <https://doi.org/10.1016/j.jhydrol.2020.125156>, 2020c.

569 Chen, Y., Huang, J., Sheng, S., Mansaray, L. R., Liu, Z., Wu, H., and Wang, X.: A new
570 downscaling-integration framework for high-resolution monthly precipitation estimates:
571 Combining rain gauge observations, satellite-derived precipitation data and geographical ancillary
572 data, *Remote Sensing of Environment*, 214, 154-172, <https://doi.org/10.1016/j.rse.2018.05.021>,
573 2018.

574 Duan, Z. and Bastiaanssen, W. G. M.: First results from Version 7 TRMM 3B43 precipitation product
575 in combination with a new downscaling–calibration procedure, *Remote Sensing of Environment*,
576 131, 1-13, <https://doi.org/10.1016/j.rse.2012.12.002>, 2013.

577 Elnashar, A., Zeng, H., Wu, B., Zhang, N., Tian, F., Zhang, M., Zhu, W., Yan, N., Chen, Z., Sun, Z., Wu,
578 X., and Li, Y.: Downscaling TRMM Monthly Precipitation Using Google Earth Engine and Google
579 Cloud Computing, *Remote Sensing*, 12, 10.3390/rs12233860, 2020.

580 Fan, D., Wu, H., Dong, G., Jiang, X., and Xue, H.: A Temporal Disaggregation Approach for TRMM
581 Monthly Precipitation Products Using AMSR2 Soil Moisture Data, *Remote Sensing*, 11,
582 10.3390/rs11242962, 2019.

583 Funk, C., Peterson, P., Landsfeld, M., Pedreros, D., Verdin, J., Shukla, S., Husak, G., Rowland, J.,
584 Harrison, L., Hoell, A., and Michaelsen, J.: The climate hazards infrared precipitation with
585 stations—a new environmental record for monitoring extremes, *Scientific Data*, 2, 150066,

586 10.1038/sdata.2015.66, 2015.

587 Gebregiorgis, A. S. and Hossain, F.: Understanding the Dependence of Satellite Rainfall Uncertainty on
588 Topography and Climate for Hydrologic Model Simulation, *IEEE Transactions on Geoscience and*
589 *Remote Sensing*, 51, 704-718, 10.1109/TGRS.2012.2196282, 2013.

590 Goovaerts, P.: Geostatistical approaches for incorporating elevation into the spatial interpolation of
591 rainfall, *J. Hydrol.*, 228, 113-129, 2000.

592 Haile, A. T., Habib, E., and Rientjes, T.: Evaluation of the climate prediction center (CPC) morphing
593 technique (CMORPH) rainfall product on hourly time scales over the source of the Blue Nile River,
594 *Hydrological Processes*, 27, 1829-1839, <https://doi.org/10.1002/hyp.9330>, 2013.

595 Hengl, T., Nussbaum, M., Wright, M. N., Heuvelink, G. B., and Gräler, B. J. P.: Random forest as a
596 generic framework for predictive modeling of spatial and spatio-temporal variables, *PeerJ*, 6,
597 e5518, 2018.

598 Hou, A. Y., Kakar, R. K., Neeck, S., Azarbarzin, A. A., Kummerow, C. D., Kojima, M., Oki, R.,
599 Nakamura, K., and Iguchi, T.: The Global Precipitation Measurement Mission, *Bulletin of the*
600 *American Meteorological Society*, 95, 701-722, 10.1175/bams-d-13-00164.1, 2014.

601 Huffman, G., Bolvin, D., Braithwaite, D., Hsu, K., and Joyce, R.: Algorithm theoretical basis document
602 (ATBD) NASA global precipitation measurement (GPM) integrated multi-satellitE Retrievals for
603 GPM (IMERG). Nasa (December), 29., 2019.

604 Huffman, G. J., Bolvin, D. T., Nelkin, E. J., Wolff, D. B., Adler, R. F., Gu, G., Hong, Y., Bowman, K. P.,
605 and Stocker, E. F.: The TRMM Multisatellite Precipitation Analysis (TMPA): Quasi-Global,
606 Multiyear, Combined-Sensor Precipitation Estimates at Fine Scales, *Journal of Hydrometeorology*,
607 8, 38-55, 10.1175/jhm560.1, 2007.

608 Immerzeel, W. W., Rutten, M. M., and Droogers, P.: Spatial downscaling of TRMM precipitation using
609 vegetative response on the Iberian Peninsula, *Remote Sensing of Environment*, 113, 362-370,
610 <https://doi.org/10.1016/j.rse.2008.10.004>, 2009.

611 Jia, S., Zhu, W., Lü, A., and Yan, T.: A statistical spatial downscaling algorithm of TRMM precipitation
612 based on NDVI and DEM in the Qaidam Basin of China, *Remote Sensing of Environment*, 115,
613 3069-3079, 10.1016/J.RSE.2011.06.009, 2011.

614 Jing, W., Yang, Y., Yue, X., and Zhao, X.: A Spatial Downscaling Algorithm for Satellite-Based
615 Precipitation over the Tibetan Plateau Based on NDVI, DEM, and Land Surface Temperature,
616 *Remote Sensing*, 8, 10.3390/rs8080655, 2016.

617 Karbalaye Ghorbanpour, A., Hessels, T., Moghim, S., and Afshar, A.: Comparison and assessment of
618 spatial downscaling methods for enhancing the accuracy of satellite-based precipitation over Lake
619 Urmia Basin, *Journal of Hydrology*, 596, 126055, <https://doi.org/10.1016/j.jhydrol.2021.126055>,
620 2021.

621 Li, M. and Shao, Q.: An improved statistical approach to merge satellite rainfall estimates and
622 raingauge data, *Journal of Hydrology*, 385, 51-64, <https://doi.org/10.1016/j.jhydrol.2010.01.023>,
623 2010.

624 Li, T., Shen, H., Yuan, Q., Zhang, X., and Zhang, L.: Estimating ground - level PM2.5 by fusing
625 satellite and station observations: a geo-intelligent deep learning approach, *Geophysical Research*
626 *Letters*, 44, 11,985-911,993, 2017.

627 Li, Y., Zhang, Y., He, D., Luo, X., and Ji, X.: Spatial Downscaling of the Tropical Rainfall Measuring
628 Mission Precipitation Using Geographically Weighted Regression Kriging over the Lancang River
629 Basin, China, *Chinese Geographical Science*, 29, 446-462, 10.1007/s11769-019-1033-3, 2019.

630 Lu, X., Tang, G., Wang, X., Liu, Y., Wei, M., and Zhang, Y.: The Development of a Two-Step Merging
631 and Downscaling Method for Satellite Precipitation Products, *Remote Sensing*, 12,
632 10.3390/rs12030398, 2020.

633 Lu, X., Tang, G., Wang, X., Liu, Y., Jia, L., Xie, G., Li, S., and Zhang, Y.: Correcting GPM IMERG
634 precipitation data over the Tianshan Mountains in China, *Journal of Hydrology*, 575, 1239-1252,
635 10.1016/J.JHYDROL.2019.06.019, 2019.

636 Ma, Z., Shi, Z., Zhou, Y., Xu, J., Yu, W., and Yang, Y.: A spatial data mining algorithm for downscaling
637 TMPA 3B43 V7 data over the Qinghai–Tibet Plateau with the effects of systematic anomalies
638 removed, *Remote Sensing of Environment*, 200, 378-395, 2017.

639 Mohsenzadeh Karimi, S., Kisi, O., Porrajabali, M., Rouhani-Nia, F., and Shiri, J.: Evaluation of the
640 support vector machine, random forest and geo-statistical methodologies for predicting long-term
641 air temperature, *ISH Journal of Hydraulic Engineering*, 26, 376-386,
642 10.1080/09715010.2018.1495583, 2020.

643 Park, N.-W., Kyriakidis, P. C., and Hong, S.: Geostatistical Integration of Coarse Resolution Satellite
644 Precipitation Products and Rain Gauge Data to Map Precipitation at Fine Spatial Resolutions,
645 *Remote Sensing*, 9, 255, 2017.

646 Pham, B. T., Le, L. M., Le, T.-T., Bui, K.-T. T., Le, V. M., Ly, H.-B., and Prakash, I.: Development of
647 advanced artificial intelligence models for daily rainfall prediction, *Atmospheric Research*, 237,
648 104845, <https://doi.org/10.1016/j.atmosres.2020.104845>, 2020.

649 R. Lima, C. H., Kwon, H.-H., and Kim, Y.-T.: A Bayesian Kriging Model Applied for Spatial
650 Downscaling of Daily Rainfall from GCMs, *Journal of Hydrology*, 126095,
651 <https://doi.org/10.1016/j.jhydrol.2021.126095>, 2021.

652 Sharifi, E., Saghafian, B., and Steinacker, R.: Downscaling Satellite Precipitation Estimates With
653 Multiple Linear Regression, Artificial Neural Networks, and Spline Interpolation Techniques,
654 *Journal of Geophysical Research Atmospheres*, 124, 789-805,
655 <https://doi.org/10.1029/2018JD028795>, 2019.

656 Shi, Y., Song, L., Xia, Z., Lin, Y., Myneni, R. B., Choi, S., Wang, L., Ni, X., Lao, C., and Yang, F.:
657 Mapping Annual Precipitation across Mainland China in the Period 2001–2010 from TRMM3B43
658 Product Using Spatial Downscaling Approach, *Remote Sensing*, 7, 5849-5878, 2015.

659 Shortridge, A. and Messina, J.: Spatial structure and landscape associations of SRTM error, *Remote
660 Sensing of Environment*, 115, 1576-1587, <https://doi.org/10.1016/j.rse.2011.02.017>, 2011.

661 Spracklen, D. V., Arnold, S. R., and Taylor, C. M.: Observations of increased tropical rainfall preceded
662 by air passage over forests, *Nature*, 489, 282-285, 10.1038/nature11390, 2012.

663 Sun, L. and Lan, Y.: Statistical downscaling of daily temperature and precipitation over China using
664 deep learning neural models: Localization and comparison with other methods, *International
665 Journal of Climatology*, 41, 1128-1147, <https://doi.org/10.1002/joc.6769>, 2021.

666 Tao, Y., Gao, X., Hsu, K., Sorooshian, S., and Ihler, A.: A Deep Neural Network Modeling Framework
667 to Reduce Bias in Satellite Precipitation Products, *Journal of Hydrometeorology*, 17, 931-945,
668 10.1175/jhm-d-15-0075.1, 2016.

669 Trenberth, K. E. and Shea, D. J.: Relationships between precipitation and surface temperature, 32,
670 <https://doi.org/10.1029/2005GL022760>, 2005.

671 Ullah, S., Zuo, Z., Zhang, F., Zheng, J., Huang, S., Lin, Y., Iqbal, I., Sun, Y., Yang, M., and Yan, L.:
672 GPM-Based Multitemporal Weighted Precipitation Analysis Using GPM_IMERGDF Product and
673 ASTER DEM in EDBF Algorithm, *Remote Sensing*, 12, 10.3390/rs12193162, 2020.

674 Wu, H., Yang, Q., Liu, J., and Wang, G.: A spatiotemporal deep fusion model for merging satellite and
675 gauge precipitation in China, *Journal of Hydrology*, 584, 124664,
676 <https://doi.org/10.1016/j.jhydrol.2020.124664>, 2020.

677 Wu, T., Feng, F., Lin, Q., and Bai, H.: Advanced Method to Capture the Time-Lag Effects between
678 Annual NDVI and Precipitation Variation Using RNN in the Arid and Semi-Arid Grasslands, *Water*,
679 11, 1789, 2019.

680 Wu, Z., Zhang, Y., Sun, Z., Lin, Q., and He, H.: Improvement of a combination of TMPA (or IMERG)
681 and ground-based precipitation and application to a typical region of the East China Plain, *Science
682 of The Total Environment*, 640-641, 1165-1175, <https://doi.org/10.1016/j.scitotenv.2018.05.272>,
683 2018.

684 Xie, P. and Xiong, A.-Y.: A conceptual model for constructing high-resolution gauge-satellite merged
685 precipitation analyses, *Journal of Geophysical Research: Atmospheres*, 116,
686 <https://doi.org/10.1029/2011JD016118>, 2011.

687 Xu, S., Wu, C., Wang, L., Gonsamo, A., Shen, Y., and Niu, Z.: A new satellite-based monthly
688 precipitation downscaling algorithm with non-stationary relationship between precipitation and
689 land surface characteristics, *Remote Sensing of Environment*, 162, 119-140,
690 <https://doi.org/10.1016/j.rse.2015.02.024>, 2015.

691 Xu, Y. and Goodacre, R.: On Splitting Training and Validation Set: A Comparative Study of
692 Cross-Validation, Bootstrap and Systematic Sampling for Estimating the Generalization
693 Performance of Supervised Learning, *J Anal Test*, 2, 249-262, 10.1007/s41664-018-0068-2, 2018.

694 Yan, X., Chen, H., Tian, B., Sheng, S., Wang, J., and Kim, J.-S.: A Downscaling–Merging Scheme for
695 Improving Daily Spatial Precipitation Estimates Based on Random Forest and Cokriging, *Remote
696 Sensing*, 13, 2040, 2021.

697 Yang, Y. and Luo, Y.: Using the Back Propagation Neural Network Approach to Bias Correct TMPA
698 Data in the Arid Region of Northwest China, *Journal of Hydrometeorology*, 15, 459-473,
699 10.1175/jhm-d-13-041.1, 2014.

700 Yang, Z., Hsu, K., Sorooshian, S., Xu, X., Braithwaite, D., Zhang, Y., and Verbist, K. M. J.: Merging
701 high - resolution satellite - based precipitation fields and point - scale rain gauge
702 measurements—A case study in Chile, *Journal of Geophysical Research: Atmospheres*, 122,
703 5267-5284, 10.1002/2016JD026177, 2017.

704 Zhang, L., Li, X., Zheng, D., Zhang, K., Ma, Q., Zhao, Y., and Ge, Y.: Merging multiple satellite-based
705 precipitation products and gauge observations using a novel double machine learning approach,
706 *Journal of Hydrology*, 594, 10.1016/J.JHYDROL.2021.125969, 2021.

707 Zhang, X. and Tang, Q.: Combining satellite precipitation and long-term ground observations for
708 hydrological monitoring in China, *Journal of Geophysical Research: Atmospheres*, 120, 6426-6443,
709 <https://doi.org/10.1002/2015JD023400>, 2015.

710 Zhao, N., Yue, T., Chen, C., Zhao, M., and Fan, Z.: An improved statistical downscaling scheme of
711 Tropical Rainfall Measuring Mission precipitation in the Heihe River basin, China, *International
712 Journal of Climatology*, 38, 3309-3322, <https://doi.org/10.1002/joc.5502>, 2018.

713 Zhao, T. and Yatagai, A.: Evaluation of TRMM 3B42 product using a new gauge-based analysis of
714 daily precipitation over China, *International Journal of Climatology*, 34, 2749-2762,
715 <https://doi.org/10.1002/joc.3872>, 2014.

716